Transition-metal oxides with peak oxygen vacancy content for oxygen electrocatalysis

Yuan Wang[1], Yu Han[1], Weiran Suo[1], Jieling Zhang[2], Xiaoyong Lai[3], Zhimin Li[1*], Zuozhong Liang[2*] and Guozhong Cao[4*]

ABSTRACT Introducing oxygen vacancies in transition-metal oxides is an effective method to improve electrocatalytic water oxidation activity. However, controlled defect engineering in metal oxides remains a challenge. In this study, high oxygen vacancy content is achieved in transition-metal oxides by regulating the pyrolysis temperature of corresponding metal hydroxides. Specifically, Co_3O_4 nanoflowers with a large amount of oxygen vacancies were obtained by pyrolysis of $Co(OH)_2$ in air at 400°C. The high oxygen vacancy content may be due to the rich porous structure and atomic rearrangement of Co and O. Electrochemical results showed that oxygen vacancy defect-rich Co_3O_4 prepared at 400°C (Co_3O_4-400) has the lowest overpotential η of 321 mV for oxygen evolution reaction at a current density j of 10 mA cm^{-2} in 1.0 mol L^{-1} KOH compared with Co_3O_4-300 (348 mV) and Co_3O_4-500 (366 mV). Theoretical calculations and experiments verified the beneficial effect of oxygen vacancies in Co_3O_4. This study offers an efficient strategy to develop highly active transition-metal oxides with optimized oxygen vacancies.

Keywords: oxygen vacancy, transition-metal oxides, oxygen evolution reaction (OER), oxygen reduction reaction (ORR), Zn-air battery

INTRODUCTION

Developing suitable catalysts to improve the kinetics and efficiency of water splitting reactions is crucial to achieving clean hydrogen [1–14]. At present, transition-metal oxides have become promising electrocatalysts for oxygen evolution reaction (OER) [15–18]. Moreover, introducing oxygen vacancies in transition-metal oxides has been confirmed as an efficient approach to tuning the coordination environment and electronic structure of metal active sites, thus improving electrocatalytic OER activity [19–22]. For instance, Wang's group [23] indicated that oxygen vacancies can help form the Co–OOH intermediate during the OER process. Recently, Zhang *et al.* [24] further explored the effect of oxygen vacancies and cobalt vacancies in Co_3O_4 for OER. Thus, introducing oxygen vacan-

cies is key to designing efficient transition-metal oxides.

Various methods have been reported to introduce oxygen vacancies, including pyrolysis [25], argon plasma treatment [26,27], physical laser fragmentation [28], $NaBH_4$ reduction [29], cation exchange reaction [30], and argon-ion irradiation [31]. However, these strategies cannot effectively control the content of vacancies. Recently, Li's group [32] reported a lithium reduction method to produce vacancies in TiO_2, ZnO, SnO_2, and CeO_2. This method can control the content of vacancies by tuning the introduction of lithium. Nevertheless, the resulting Li_2O needs to be removed by an acid leaching process.

In this study, a simple and universal method for preparing oxygen vacancy defect-rich transition-metal oxides is reported. Transition-metal hydroxides were synthesized and calcined in air, followed by thermogravimetric analysis (TGA). A series of nanostructured porous Co_3O_4 with abundant oxygen vacancies was obtained at different calcination temperatures. The optimized Co_3O_4 exhibited excellent bifunctional OER and oxygen reduction reaction (ORR) capabilities. The Co_3O_4-based Zn-air battery demonstrated a discharge/charge voltage gap and good long-term stability. Theoretical calculation was performed to understand the intrinsic structure changes of Co_3O_4 with oxygen vacancies. This work offers new insights into developing oxygen vacancy defect-rich and highly efficient transition-metal oxide-based electrocatalysts.

EXPERIMENTAL SECTION

Material synthesis

The $Co(OH)_2$ precursor was prepared based on a previous method [33]. The precursor was pyrolyzed in a muffle oven at 300, 350, 400, 450, and 500°C for 2 h. Similar pyrolysis was performed for commercial Co-, Ni-, and Cu-based hydroxides.

Material characterization

Crystal structures were analyzed by a powder X-ray diffractometer (XRD, D8 Advance, Bruker). Morphologies were characterized by scanning electron microscopy (SEM, Hitachi, TM3000) and transmission electron microscopy (TEM, JEOL JEM-2100F). Nitrogen adsorption and desorption curves were

[1] School of Advanced Materials and Nanotechnology, Xidian University, Xi'an 710126, China
[2] Key Laboratory of Applied Surface and Colloid Chemistry, Ministry of Education, School of Chemistry and Chemical Engineering, Shaanxi Normal University, Xi'an 710119, China
[3] State Key Laboratory of High-efficiency Utilization of Coal and Green Chemical Engineering, College of Chemistry and Chemical Engineering, Ningxia University, Yinchuan 750021, China
[4] Department of Materials Science and Engineering, University of Washington, Seattle, Washington 98195-2120, USA
* Corresponding authors (emails: zmli@mail.xidian.edu.cn (Li Z); liangzuozhong@snnu.edu.cn (Liang Z); gzcao@u.washington.edu (Cao G))

recorded using an AutosorbiQ surface area analyzer (ASAP2020, Micromeritics). X-ray photoelectron spectroscopy (XPS) was conducted using an X-ray photoelectron spectrometer (AXIS ULTRA, Kratos Analytical Ltd.). Electron paramagnetic resonance (EPR) spectra were collected using a spectrometer (Bruker, ELEXSYS E500 plus) at 9.43 GHz. Contact angles were determined using a contact angle meter (OCA20, DataPhysics). Electrical conductivities were measured with a four-terminal powder resistivity tester (ST2722-SD) and high-resistance microcurrent tester (ST2643) at a temperature of 28°C and humidity of 45% relative humidity (RH) with the pressure range of the powder analyzer of 2–20 MPa. The conductivity results measured at the pressure of 2 MPa were selected for comparison.

Electrochemical tests

Electrochemical OER activities were measured with a CHI 630E electrochemical workstation in 1.0 mol L^{-1} KOH. A glass carbon (GC, 0.07 cm^2) electrode was selected as the working electrode. The carbon rod was selected as the counter electrode. The Ag/AgCl electrode was selected as the reference electrode. The Co_3O_4 catalyst (4.0 mg) was placed in a centrifuge tube containing ethanol (320 μL), deionized water (640 μL), and Nafion (40 μL, 5 wt%). The above catalyst ink (5 μL) was loaded on the GC electrode. Linear sweep voltammetry (LSV) data were acquired at 0.01 V s^{-1}. Tafel slopes were determined at 0.002 V s^{-1}. All cyclic voltammetry (CV), LSV, and Tafel data were corrected with 100% iR compensation. Electrochemical impedance spectroscopy (EIS) was performed at 1.55 V ($vs.$ reversible hydrogen electrode (RHE)) (0.1–100 kHz). Faraday efficiency was obtained using a closed H-type cell and a standard three-electrode system. Co_3O_4-400-coated carbon cloth (1 cm × 1 cm) was used as the working electrode. Controlled current electrolysis was performed at j = 15 mA cm^{-2} for 50 min. Gaseous products were withdrawn from the headspace of the H-type cell via a gas-tight syringe every 10 min and analyzed with a Shimadzu GC-2014 gas chromatography system equipped with Shimadzu Molecular Sieve 5A (80/100 mesh 3.2 mm × 2.1 mm × 2.0 m). Furthermore, the oven temperature was kept at 60°C. A thermal conductivity detector was used to detect O_2. Nitrogen was used as the carrier gas. Long-term stability measurements were performed at 1.65 V ($vs.$ RHE). The overpotential η was calculated using Equation (1).

$$\eta = E_{Ag/AgCl} + 0.059 \times pH + 0.197 - 1.23 \text{ V}, \tag{1}$$

where $E_{Ag/AgCl}$ is the Ag/AgCl electrode potential.

Electrochemical surface area (ECSA) values were calculated using Equation (2).

$$ECSA = C_{dl}/C_s, \tag{2}$$

where C_{dl} is the slope of Δj $vs.$ v (scan rate) and C_s is the specific capacitance of Co-based catalysts (~27 μF cm^{-2}). Turnover frequency (TOF) values were calculated using Equation (3).

$$TOF = i/4 \times n \times F, \tag{3}$$

where i is the measured current at η = 350 mV, n is the number of moles of all Co_3O_4 catalysts coated on the GC electrode, and F is Faraday's constant (96,485 C mol^{-1}). Assuming that all Co_3O_4 catalysts participate in the OER process,

$$n = V_{GC} \times m/V \times M, \tag{4}$$

where V_{GC} is the volume of catalyst coated on the GC electrode (5 μL), m is the mass of catalyst ink (4 mg), V is the volume of catalyst ink (1 mL), and M is the molar weight of Co_3O_4 (241 g mol^{-1}).

Diffusion coefficients of rate-limiting species (D_0, cm^2 s^{-1})

were computed using the Randles–Sevcik equation (Equation (4)).

$$i_P = 2.69 \times 10^5 n^{3/2} D_0^{1/2} v^{1/2} A C_0, \tag{5}$$

where i_p is the peak current (A), n is the electron transfer number (usually 1), A is the surface area of the GC electrode (0.07 cm^{-2}), and C_0 is the concentration of the measured catalyst (0.025 mol cm^{-3}).

Electrochemical ORR activities were measured with a CHI 760E electrochemical workstation in O_2-saturated 0.1 mol L^{-1} KOH. A rotating ring-disk electrode (RRDE) was applied as the working electrode. The surface areas of the disk electrode and Pt ring electrode were 0.247 and 0.186 cm^2, respectively. A PINE integrated rotating disc electrode device was used for ORR measurements at high rotating speed. First, 10 mg of catalysts and 4 mg of carbon nanotubes were dispersed in a mixed solution of ethanol (320 μL) and deionized water (640 μL) containing Nafion (40 μL, 5 wt%). Subsequently, the above catalyst ink (20 μL) was coated on the RRDE. LSV curves were collected at 1600 r min^{-1} and 0.01 V s^{-1}. Tafel slopes were calculated from the LSV measured at 0.002 V s^{-1}. The electron transfer number (n) was calculated using Equation (6).

$$n = 4 \times j_d/(j_d + j_r/N), \tag{6}$$

where j_d is the current of the disk electrode, j_r is the current of the ring electrode, and N is the collection efficiency of the Pt ring electrode (0.39).

Zn-air battery

A typical Zn-air battery comprises a Zn plate, an electrolyte, and an air electrode. Prior to use, the Zn plate was polished. The electrolyte (6.0 mol L^{-1} KOH and 0.02 mol L^{-1} $ZnCl_2$) was prepared by dissolving certain amounts of KOH and $ZnCl_2$ in deionized water. The air electrode was assembled by coating the catalysts on carbon cloth and a gas diffusion layer.

Computational simulation

Density functional theory (DFT) calculations were conducted by the CASTEP module with the Materials Studio 8.0 software package. The crystal structures of Co_3O_4 without oxygen vacancies ($Co_{24}O_{32}$) and with oxygen vacancies ($Co_{24}O_{26}$) were constructed. The generalized gradient approximation (GGA) with Perdew–Burke–Ernzerhof (PBE) and projected augmented wave (PAW) pseudopotential were applied to describe the interactions between the core and electrons. An energy cutoff of 450 eV was applied for the plane-wave expansion. A Monkhorst–Pack of k-point mesh of 4 × 4 × 4 was applied for density of states (DOS) calculations. The force and energy convergence thresholds were set to 0.01 eV Å^{-1} and 10^{-5} eV, respectively.

RESULTS AND DISCUSSION

Fig. 1a illustrates the two-step synthesis route for Co_3O_4 materials at different calcination temperatures (300–500°C). The $Co(OH)_2$ precursor was synthesized by co-precipitation with $CoSO_4$ and N_2H_4 [33]. The XRD pattern in Fig. S1 shows that pure $Co(OH)_2$ was obtained. Peaks at 12.3°, 23.5°, 33.4°, and 59.5° were assigned to the (003), (006), (012), and (110) planes of $Co(OH)_2$, respectively [34]. Fig. 1b shows the SEM image of $Co(OH)_2$ nanoflowers with the diameter of ~1 μm. In Fig. 1b$_1$, ~20-nm-thick nanosheets were aggregated into nanoflowers. The TEM image presents hollow $Co(OH)_2$ aggregates (Fig. 1b$_2$). The lattice distance of 0.23 nm is ascribed to the (102) plane of $Co(OH)_2$ (Fig. 1b$_3$). For Co_3O_4 calcined at 300°C (Co_3O_4-300),
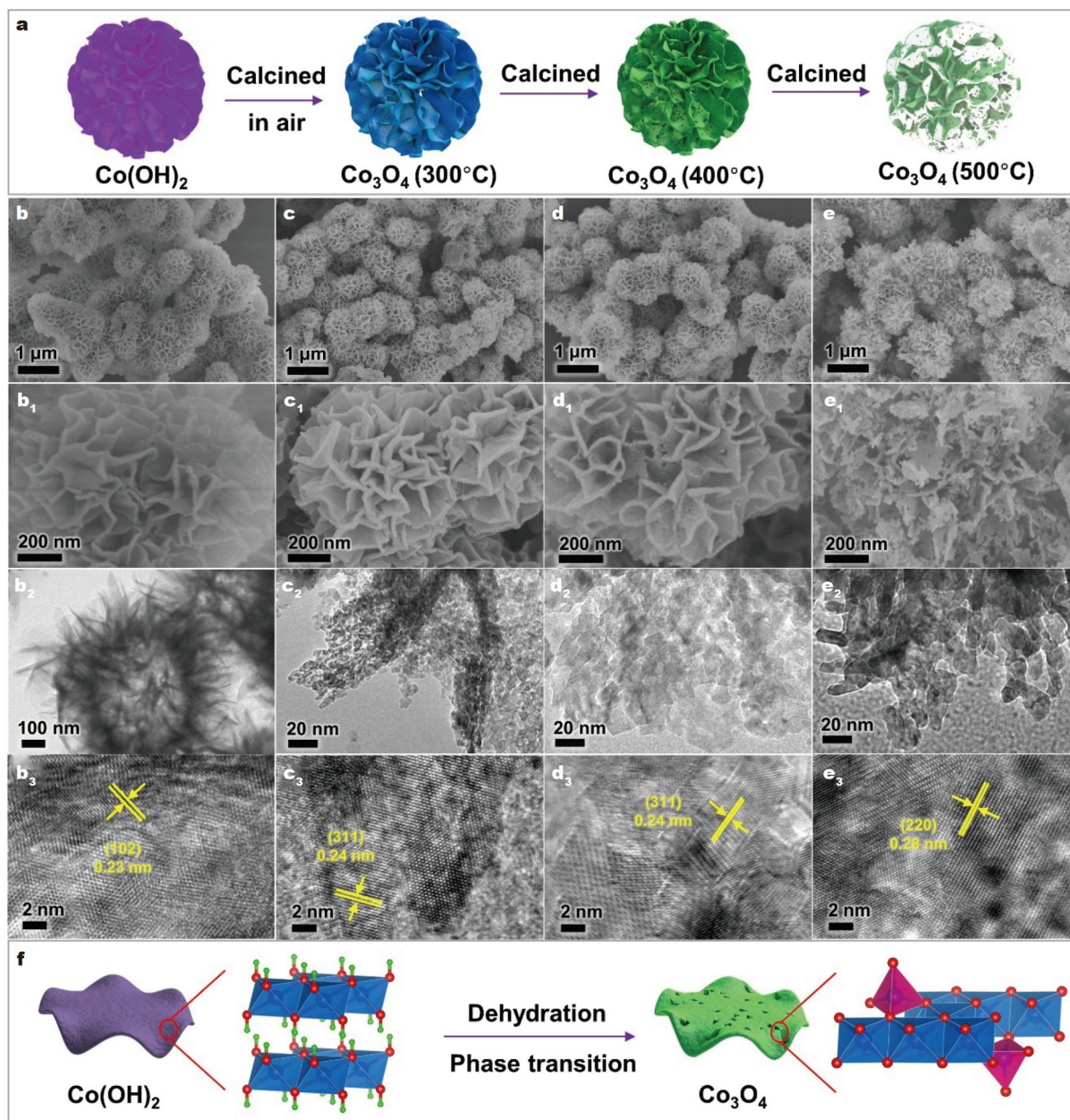
Figure 1 (a) Synthesis procedure and schematic illustration of Co(OH)$_2$ and Co$_3$O$_4$ obtained at different pyrolysis temperatures. SEM images (b–e, b$_1$–e$_1$), TEM images (b$_2$–e$_2$), and HRTEM images (b$_3$–e$_3$) of the Co(OH)$_2$ precursor (b, b$_1$–b$_3$), Co$_3$O$_4$-300 (c, c$_1$–c$_3$), Co$_3$O$_4$-400 (d, d$_1$–d$_3$), and Co$_3$O$_4$-500 (e, e$_1$–e$_3$). (f) Schematic of morphology and structure evolution from Co(OH)$_2$ to Co$_3$O$_4$.

the shape of Co(OH)$_2$ remained the same (Fig. 1c). The high-resolution TEM (HRTEM) image shows a fringe of 0.24 nm, which is assigned to the (311) plane of Co$_3$O$_4$ (Fig. 1c$_3$). Increasing the calcination temperature to 400°C did not change the morphology of Co$_3$O$_4$-400 (Fig. 1d). However, a porous structure with a pore size of ~5 nm was observed on nanosheets (Fig. 1d$_1$–d$_3$). At 500°C, the flower-like Co$_3$O$_4$-500 collapsed (Fig. 1e, e$_1$). The TEM images of Co$_3$O$_4$-500 show the formation of more Co$_3$O$_4$ nanoparticles (Fig. 1e$_2$, e$_3$). The HRTEM image shows a crystal lattice of ~0.28 nm, indexed to the (220) plane of Co$_3$O$_4$ (Fig. 1e$_3$).

N$_2$ adsorption–desorption isotherms (Fig. S2) reveal the Brunauer–Emmett–Teller (BET) surface areas of 54.4, 62.5, and 33.5 m^2 g^{-1} for Co$_3$O$_4$-300, Co$_3$O$_4$-400, and Co$_3$O$_4$-500, respec-

tively. The large surface area of Co$_3$O$_4$-400 was due to the mesoporous structure (~4 nm) of Co$_3$O$_4$ nanoflowers (Fig. S3). During the high-temperature pyrolysis process, the layered Co(OH)$_2$ precursor underwent dehydration, which led to the formation of a porous structure (Fig. 1f). Co(OH)$_2$ includes a Co ion with six coordination states, while Co$_3$O$_4$ has two Co ions with six and four coordination states. Thus, both Co and O atoms underwent atom rearrangement during the pyrolysis process from 300 to 500°C.

Furthermore, considering the TGA curve, Co(OH)$_2$ began to decompose into Co$_3$O$_4$ at 300°C (Fig. 2a). The weight loss from Co(OH)$_2$ to Co$_3$O$_4$ (~13%) is consistent with dehydration and phase transition processes. The XRD patterns of the samples prepared at 300, 400, and 500°C concur with the Co$_3$O$_4$ phase
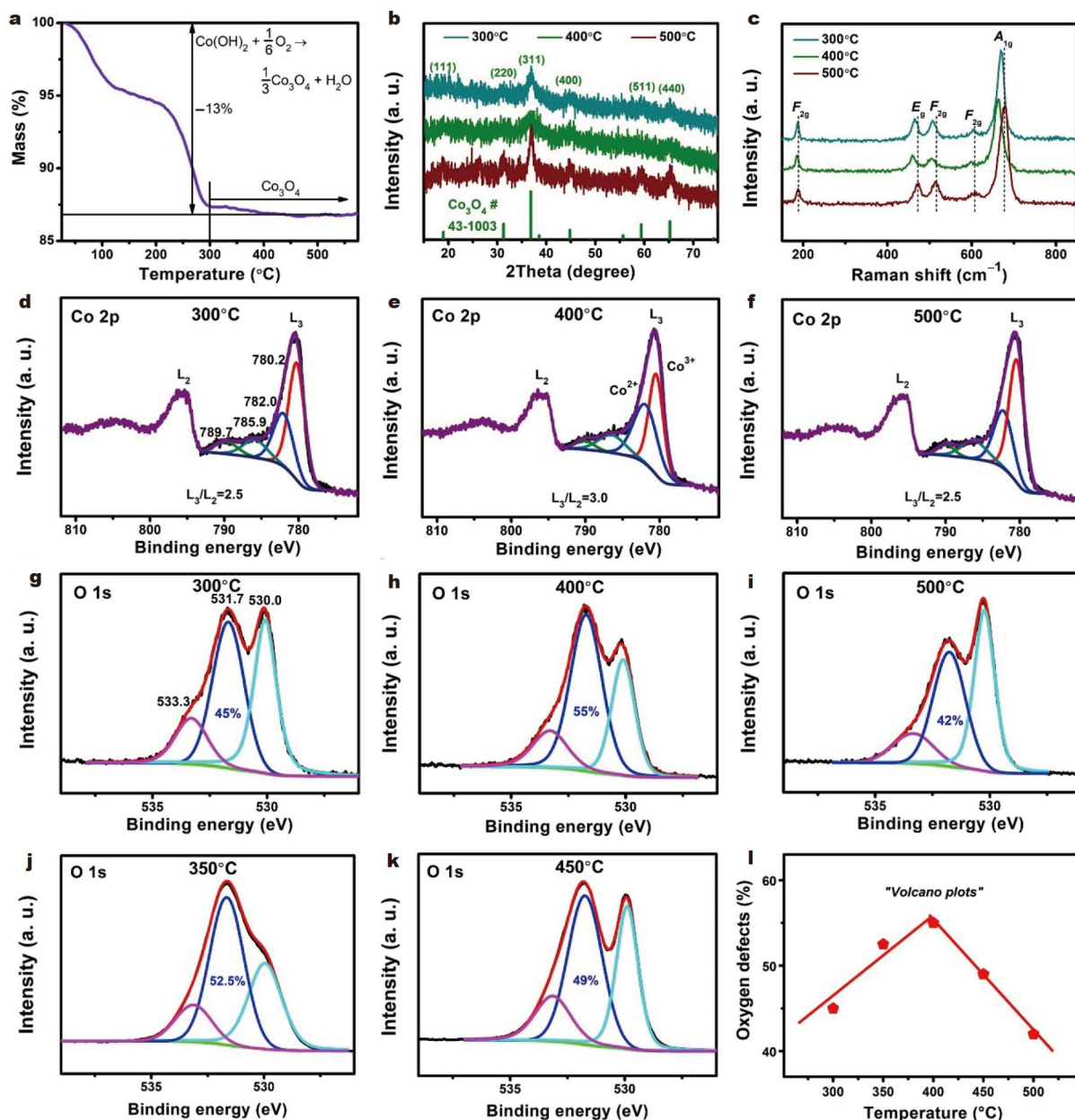
Figure 2 Weight loss curve of Co(OH)₂ (a). XRD patterns (b), Raman spectra (c), high-resolution XPS spectra of Co 2p (d–f) and O 1s (g–k) of Co₃O₄-300 (d, g), Co₃O₄-350 (j), Co₃O₄-400 (e, h), Co₃O₄-450 (k), and Co₃O₄-500 (f, i). Oxygen vacancy contents for Co₃O₄ as a function of the calcination temperature (l).

(JCPDS No. 43-1003) (Fig. 2b). Fig. 2c presents the Raman spectra of the Co₃O₄ samples. Peaks at around 188, 474, 513, 610, and 678 cm^{-1} were detected in Co₃O₄-500, which were attributed to the F_{2g}, E_g, F_{2g}, F_{2g}, and A_{1g} modes, respectively [35]. These peaks are attributed to the main Co–O vibration. It should be noted that the positions of the F_{2g}, E_g and A_{1g} peaks in Co₃O₄-400 moved to lower binding energies compared with those in Co₃O₄-300 and Co₃O₄-500, showing the formation of rich oxygen vacancies [36].

Fig. 2d–k and Fig. S4 display the high-resolution XPS spectra of Co 2p and O 1s. Co₃O₄-400 shows the highest L_3/L_2 ratio (the white line intensity ratio of Co L_3/L_2; L_3 and L_2 lines are the transitions from $2p^{3/2}$ to $3d^{3/2}3d^{5/2}$ and from $2p^{1/2}$ to $3d^{3/2}$, respectively) (3.0) compared with Co₃O₄-300 (2.5), Co₃O₄-350 (2.78), Co₃O₄-450 (2.75), and Co₃O₄-500 (2.5), indicating the

presence of more oxygen vacancies in Co₃O₄-400 [37–39]. The XPS spectrum of Co $2p_{3/2}$ was fitted with two peaks at 780.2 and 782.0 eV, which are ascribed to the Co^{3+} and Co^{2+} species, respectively [40]. Two satellite peaks appear at 785.9 and 789.7 eV. From the XPS results, the Co^{2+}/Co^{3+} ratio for Co₃O₄ prepared at 400°C is ~1.0, while those for Co₃O₄ prepared at both 300 and 500°C are only ~0.60. In general, a higher Co^{2+}/Co^{3+} indicates more oxygen vacancies [29], which further verifies the presence of higher oxygen vacancy density in Co₃O₄-400. Moreover, the high-resolution O 1s XPS spectrum reveals three peaks (Fig. 2g): ~530.0 eV ascribed to the lattice oxygen, ~533.0 eV attributed to surface-adsorbed hydroxyl species [41], and ~531.7 eV caused by the chemisorption of oxygen vacancies, which is a typical feature of oxygen vacancies [37]. In this work, the Co₃O₄ samples prepared at 300–500°C show similar peaks in

the O 1s spectra. The peak area of Co_3O_4-400 at 531.7 eV is 55%, which is the largest value compared with Co_3O_4-300 (45%), Co_3O_4-350 (52.5%), Co_3O_4-450 (49%), and Co_3O_4-500 (42%) (Fig. 2g–k), confirming the maximum content of oxygen vacancies in Co_3O_4-400. Fig. 2l shows that the oxygen vacancy content of Co_3O_4 increases first and then decreases with increasing the calcination temperature. The XRD pattern of Co_3O_4-400 also implies rich vacancies. EPR was conducted to further confirm the formation of oxygen vacancies [42,43]. Compared with Co_3O_4-300 and Co_3O_4-500, Co_3O_4-400 shows a strong peak at 2750 G, indicating the presence of more oxygen vacancies in Co_3O_4-400 (Fig. S5). Thus, a maximum oxygen vacancy content was obtained for Co_3O_4-400 during the pyrolysis process.

To explore the universality of this pyrolysis strategy with different temperatures, commercial Co-, Ni-, and Cu-based hydroxides were selected. The peak oxygen vacancy content was studied during the calcination process in the air (Fig. 3 and Figs S6–S8). The XRD patterns confirm the crystal phases of the commercial metal hydroxides, as shown in Fig. 3a–c. Calcination temperature was determined from the TGA curves (Fig. 3a$_1$–c$_1$). These metal hydroxides show micron-sized spherical morphologies (insets of Fig. 3a$_1$–c$_1$). Calcination of these three metal hydroxides was conducted at >400°C in air under the same conditions as above. The XRD patterns confirm the formation of the corresponding metal oxides (Fig. 3a$_3$–c$_3$). The XPS spectra of O 1s for the Co-, Ni-, and Cu-based oxides were recorded (Fig. 3a$_2$–c$_2$ and Figs S6–S8). High oxygen vacancy contents for these three metal oxides were observed (Fig. 3a$_2$–c$_2$). The formation of oxygen vacancy defect-rich Co_3O_4 was also detected
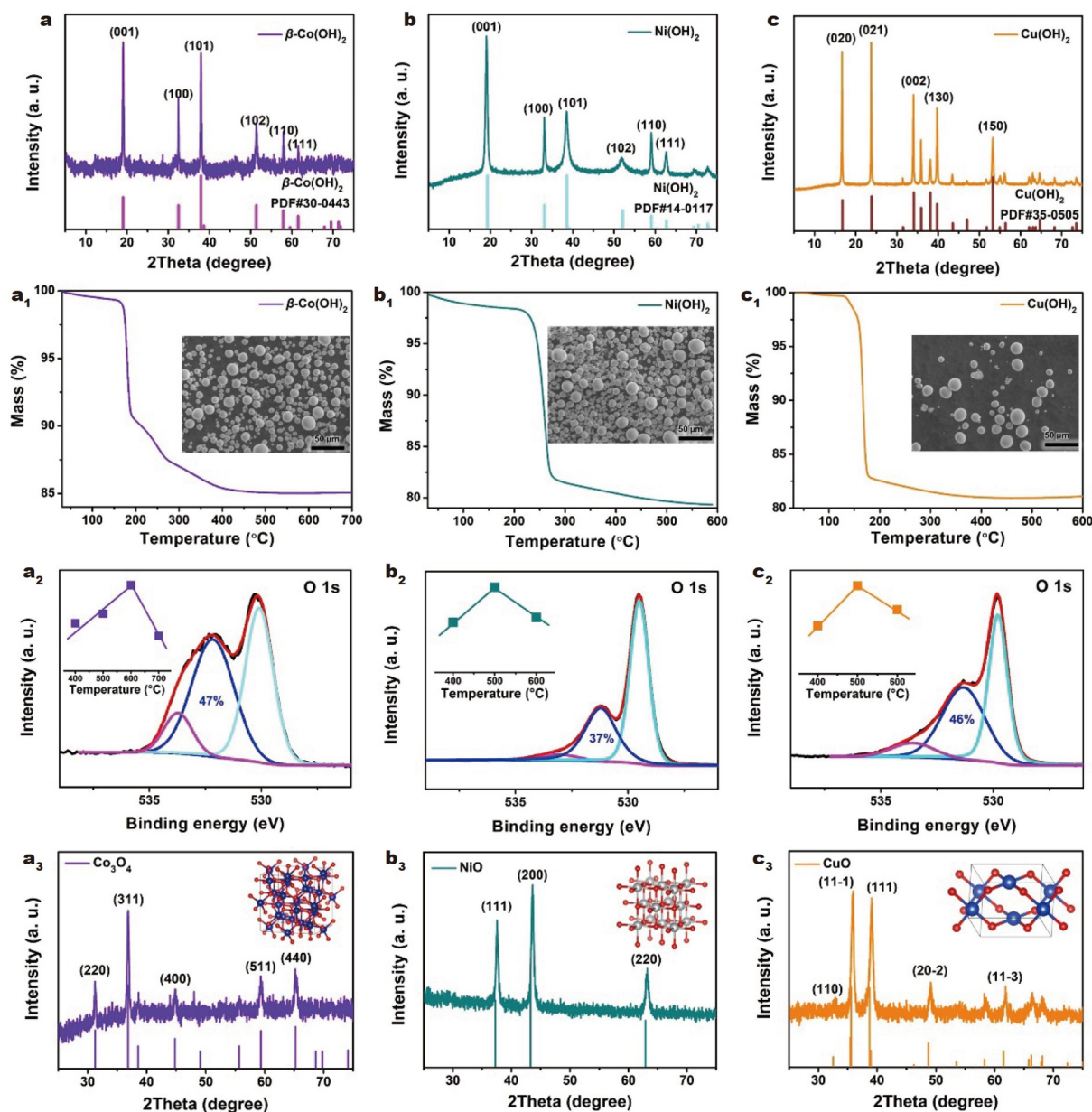
Figure 3 XRD patterns (a–c), TGA curves (a$_1$–c$_1$), and SEM images (insets of a$_1$–c$_1$) of commercial transition-metal-based hydroxides β-Co(OH)$_2$, Ni(OH)$_2$, and Co(OH)$_2$. XPS spectra of O 1s (a$_2$–c$_2$), volcano plots of oxygen vacancy contents (insets of a$_2$–c$_2$), XRD patterns (a$_3$–c$_3$), and crystal structures (insets of a$_3$–c$_3$) for the Co-based oxides obtained at 600°C (a$_2$, a$_3$), Ni-based oxides obtained at 500°C (b$_2$, b$_3$), and Cu-based oxides obtained at 500°C (c$_2$, c$_3$).

from the commercial β-Co(OH)$_2$ precursor. Both Ni(OH)$_2$ and Cu(OH)$_2$ underwent dehydration during the pyrolysis process. Based on the crystal structures of Ni(OH)$_2$ and NiO, the coordination number of Ni still remained six after the calcination. The optimized content of oxygen vacancies for NiO is relatively small (37%), which is caused by the collapse of structures during the dehydration process. Conversely, Cu atoms experienced both dehydration and phase transition with the change in coordination number from six (Cu(OH)$_2$) to five (CuO). The optimized content of oxygen vacancy for CuO is relatively large (46%) and similar to that for Co$_3$O$_4$ (47%). Some groups synthesized CoO materials with optimized oxygen vacancy contents by pyrolyzing the corresponding hydroxides [37,44]. Thus, the peak oxygen vacancy content for transition-metal oxides may be a common phenomenon when pyrolyzing metal hydroxides at high temperature. Usually, oxygen vacancies are acquired in an oxygen-deficit atmosphere such as vacuum, Ar, and N$_2$ environment because the formation mechanism of oxygen vacancy involves oxygen atom escape in metal oxides from the lattice at high temperature in an oxygen-deficit atmosphere [45]. However, it is demonstrated that relatively more oxygen vacancies are obtained by pyrolysis in an oxygen-deficit atmosphere than in an oxygen-rich atmosphere [45]. Our previous work reveals that the oxygen vacancy content for CoO obtained in Ar is 58% [44], which is larger than that for Co$_3$O$_4$ (55%) obtained in the air in this work. Moreover, the oxygen vacancy content should increase monotonically with increasing temperature. However, during the pyrolysis process, mesoporous structures were observed due to the dehydration and phase transition process, which can hinder ion diffusion. Furthermore, the metal atoms and oxygen atoms underwent atomic rearrangement due to the change in coordination environment, as confirmed by the weak XRD diffraction peaks of Co$_3$O$_4$ obtained at 400°C. Similar results were also observed [37]. Thus, the dehydration process and formation of mesoporous structures play a crucial role in determining the peak oxygen vacancy content.

Fig. 4 shows the OER activities of Co$_3$O$_4$ measured in 1.0 mol L^{-1} KOH. Co$_3$O$_4$-400 displayed an overpotential η of 321 mV at j = 10 mA cm^{-2}, which is smaller than that of novel metal oxide RuO$_2$ (333 mV) [46]. Overpotentials for Co$_3$O$_4$-300 and Co$_3$O$_4$-500 were 348 and 366 mV, respectively (Fig. 4a). Thus, oxygen vacancy-rich Co$_3$O$_4$-400 presented the best OER performance. Similar results of catalytic OER activities were observed for oxygen vacancy-rich NiO (Fig. S9) and CuO (Fig. S10). In addition, the OER performance of oxygen vacancy-rich Co$_3$O$_4$-400 and other recently published Co-based oxides measured with the GC electrode were compared (Table S1). The oxygen vacancy-rich Co$_3$O$_4$-400 exhibits better OER performance than most of the other compared materials.

Moreover, Co$_3$O$_4$-400 exhibited a relatively small Tafel slope (60.7 mV dec^{-1}), while the Tafel slopes of Co$_3$O$_4$-300 and Co$_3$O$_4$-500 were 65.0 and 78.1 mV dec^{-1}, respectively (Fig. 4b). Electric double-layer capacitances (C_{dl}) were determined by CV at different scan rates (Fig. S11), as shown in Fig. 4c, followed by calculation of the ECSA. The ECSA values for Co$_3$O$_4$-300, Co$_3$O$_4$-400, and Co$_3$O$_4$-500 are 0.37, 0.46, and 0.33 cm^2, respectively, the trend of which is consistent with the BET surface areas. Normalized LSV data based on ECSA values reveals that Co$_3$O$_4$-400 has the best intrinsic activity for OER (Fig. S12).

The TOF values of Co$_3$O$_4$-300, Co$_3$O$_4$-400, and Co$_3$O$_4$-500 at

an overpotential η of 350 mV are 0.024, 0.051, and 0.013 s^{-1}, respectively. Co$_3$O$_4$-400 exhibits the highest TOF value, further showing that the oxygen vacancy structure can enhance the intrinsic activity of OER. The generated O$_2$ of Co$_3$O$_4$-400 was determined by a gas chromatography system, which indicated a Faradaic efficiency of >90% for O$_2$ production (Fig. S13). Afterward, controlled potential electrocatalysis was performed to evaluate the long-term stability. After 12 h of electrocatalysis, the current densities of the three Co$_3$O$_4$ samples were still unchanged, indicating their excellent stability (Fig. S14). The Co$_3$O$_4$-400 catalyst was characterized again after the stability test. The SEM images (Fig. S15) and TEM and HRTEM images (Fig. S16) of Co$_3$O$_4$-400 before and after the OER stability test show no obvious morphology and crystal structure change (Fig. S16). The crystal lattice spacing values of 0.21 and 0.24 nm are indexed to the (400) and (311) planes of Co$_3$O$_4$, respectively. In addition, an amorphous layer was observed on the surface of Co$_3$O$_4$-400 after the stability test (Fig. S16c, d), which was attributed to the reconstructed catalyst as reported in the literature [24]. The XPS spectrum of Co 2p$_{3/2}$ for Co$_3$O$_4$-400 after the OER stability test was fitted with two main peaks at 779.6 and 781.3 eV and one satellite peak at 789.8 eV (Fig. S17a). The increased Co^{3+}/Co^{2+} ratio and reduced satellite peak intensity both indicate the increased valence state of the surface Co species and the formation of CoOOH [24,47,48]. A new prominent peak of O 1s appears at 529.3 eV, further suggesting the presence of surface CoOOH species. This peak is generally observed in Co-based catalysts after the stability test (Fig. S17b) [44,48,49].

Typical CV current responses for the three Co$_3$O$_4$ catalysts with different scan rates (v = 0.1–2.0 V s^{-1}) were obtained to study the catalytic OER process (Figs S18–S20). Oxidation peaks at ~1.5 V (vs. RHE) are assigned to the Co^{III}/Co^{IV} of Co$_3$O$_4$ (Fig. S18), consistent with other Co-based materials used for OER [48,50]. Herein, the linear i–$v^{1/2}$ responses for the reductive peak E_1 at ~1.4 V (vs. RHE) of Co$_3$O$_4$ prepared at different temperatures indicate the diffusion-controlled OER process (Figs S18d–S20d). The D_0 for the Co$_3$O$_4$ samples were calculated. Co$_3$O$_4$-400 shows the largest D_0 (7.6 × 10^{-6} cm^2 s^{-1}) compared with Co$_3$O$_4$-300 (7.4 × 10^{-6} cm^2 s^{-1}) and Co$_3$O$_4$-500 (5.5 × 10^{-6} cm^2 s^{-1}), displaying the fastest diffusion rate of the active species for Co$_3$O$_4$-400. This result is also consistent with the porous structure and open spherical morphology. Thus, oxygen vacancy defect-rich Co$_3$O$_4$-400 shows high catalytic OER activity. Table 1 presents the electrocatalytic activities of these Co$_3$O$_4$ samples.

The ORR performance of Co$_3$O$_4$-400 was evaluated in 0.1 mol L^{-1} KOH. In the LSV curves (Fig. 4d), Co$_3$O$_4$-400 shows a half-wave potential $E_{1/2}$ of 0.80 V (vs. RHE), while Pt/C (20 wt%) has a value of 0.88 V (vs. RHE) [51]. In addition, the Tafel slope of Co$_3$O$_4$-400 is 91.7 mV dec^{-1}, which is larger than that of Pt/C (77.0 mV dec^{-1}, Fig. 4e). It is well known that the number of electrons transferred (n) for Pt/C is ~4.0, exhibiting a 4e O$_2$ reduction process. Here, Co$_3$O$_4$-400 exhibits an n value of ~3.7, indicating a dominant 4e ORR (Fig. 4f). Based on the excellent OER/ORR performance of Co$_3$O$_4$-400, the performance of the Zn-air battery was evaluated by assembling catalysts on the air cathode, as illustrated in Fig. 4g. The open circuit voltage of the Co$_3$O$_4$-400-based Zn-air battery is ~1.4 V (Fig. S21). The discharge–charge cycling test shows that the voltage band gaps of Zn-air battery constructed with Co$_3$O$_4$-400 and RuO$_2$ + Pt/C [46] are similar (~0.88 V) at j = 2 mA cm^{-2},
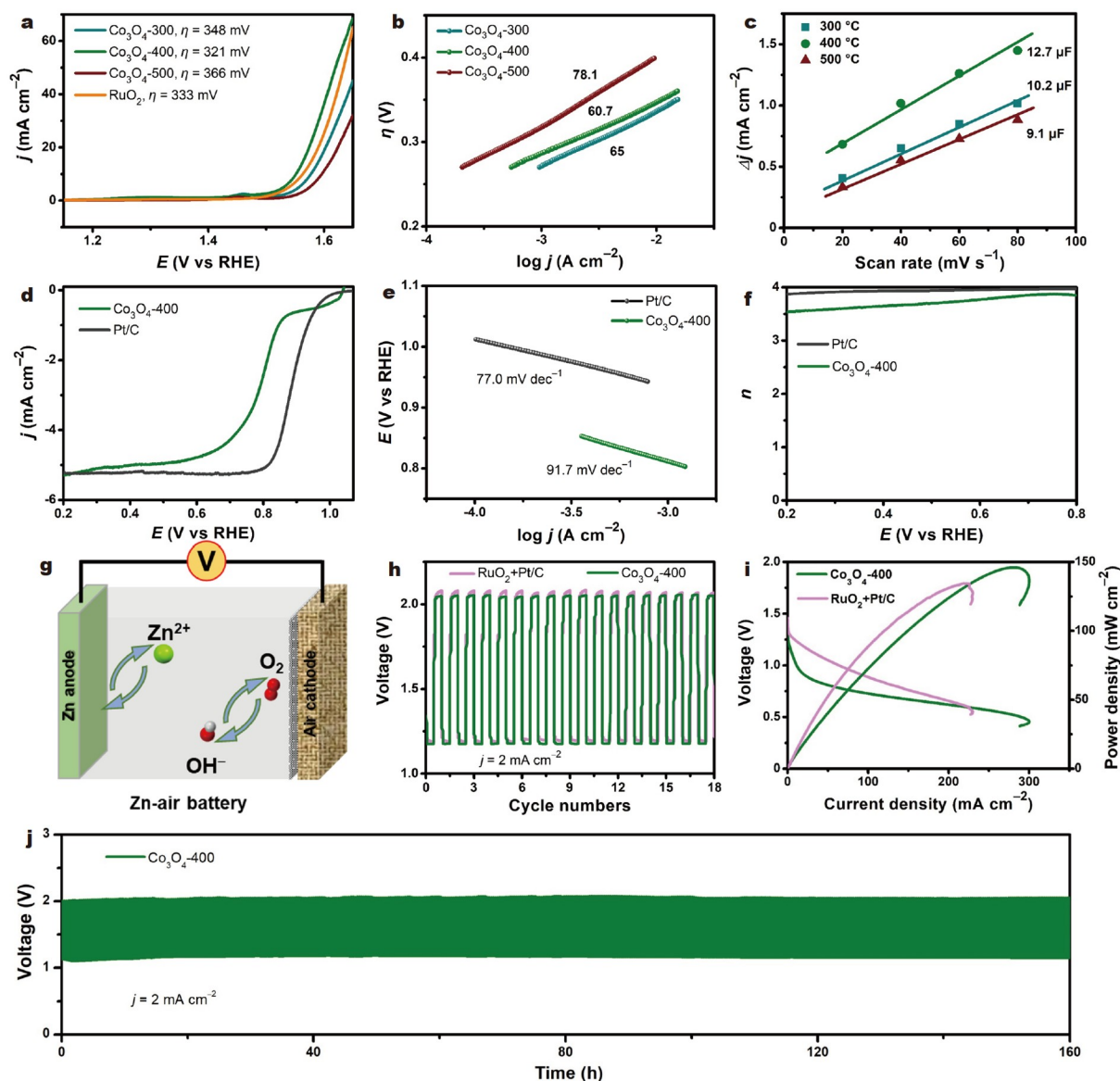
Figure 4 LSV curves (a), Tafel slopes (b), and Nyquist plots (c) of Co_3O_4-300, Co_3O_4-400, and Co_3O_4-500 and commercial RuO_2 measured in 1.0 mol L^{-1} KOH. LSV curves (d), Tafel slopes (e), and electron transfer numbers (f) of Co_3O_4-400 and commercial Pt/C (20 wt%) measured in 0.1 mol L^{-1} KOH. Schematic illustration of a Zn-air battery made of the Zn anode, the electrolyte (6.0 mol L^{-1} KOH and 0.02 mol L^{-1} $ZnCl_2$), and the catalyst cathode (g). Discharge–charge cycling test measured at $j = 2$ mA cm^{-2} (h) and discharging polarization data and power densities (i) of Co_3O_4-400 and $RuO_2 + Pt/C$. Stability test of Co_3O_4-400 measured at $j = 2$ mA cm^{-2} (j).

Table 1 Comparison of OER performance for Co_3O_4-300, Co_3O_4-400, and Co_3O_4-500

Catalysts	η at $j = 10$ mA cm^{-2} (mV)	Tafel slope (mV dec^{-1})	ECSA (cm^2)	TOF at $\eta = 350$ mV (s^{-1})	D_0 (cm^2 s^{-1})
Co_3O_4-300	348	65.0	0.37	0.024	7.4×10^{-6}
Co_3O_4-400	321	60.7	0.46	0.051	7.6×10^{-6}
Co_3O_4-500	366	78.1	0.33	0.013	5.5×10^{-6}

pointing out the excellent bifunctional OER/ORR performance (Fig. 4h). The specific capacity measured at $j = 20.0$ mA cm^{-2} is 723 mA h g^{-1} (Fig. S22). According to the discharging polarization data, the maximum power density of Co_3O_4-400 is ~146 mW cm^{-2}, which is larger than that of $RuO_2 + Pt/C$ (~134 mW cm^{-2}) (Fig. 4i). The long-term discharge–charge

stability test of Co_3O_4-400 demonstrates its excellent durability after running for 160 h without obvious decay of activity (Fig. 4j). Overall, the Co_3O_4-400-assembled Zn-air battery exhibits high activity and stability compared with the commercial noble metal-based catalysts.

DFT calculations were further performed to investigate the

effect of oxygen vacancies on the electronic structure and catalytic activity of Co_3O_4. Herein, the crystal structures of Co_3O_4 without and with oxygen vacancies were constructed (Fig. 5a, c). The total DOS (TDOS) of Co_3O_4 without oxygen vacancies confirms that Co_3O_4 is a semiconductor oxide with an obvious intrinsic bandgap (Fig. 5b). Conversely, the TDOS of Co_3O_4 with oxygen vacancies is continuous around the Fermi level (Fig. 5d). Co_3O_4 with oxygen vacancies combines the intrinsic bandgap with high conductivity. A similar phenomenon was verified in the literature [52]. Also, the conductivity test and EIS results further confirm the improvement of conductivity. Co_3O_4-400 shows the largest conductivity at 0.190 µS cm^{-1} compared with Co_3O_4-300 (0.018 µS cm^{-1}) and Co_3O_4-500 (0.013 µS cm^{-1}) measured at 2 MPa (Fig. 5e and Tables S2–S4). The electron transfer resistance of Co_3O_4-400 is the lowest compared with those of Co_3O_4-300 and Co_3O_4-500, showing the beneficial effect of oxygen vacancies on charge transfer rate (Fig. 5f). Thus, introducing oxygen vacancy defects can improve the conductivity of catalysts. Furthermore, the contact angles of the as-prepared Co_3O_4 samples were measured. Co_3O_4-400 has the smallest contact angle of 104.7° compared with Co_3O_4-300 (115.4°) and Co_3O_4-500 (120.0°) (Fig. 5g–i). Thus, the oxygen vacancy-rich Co_3O_4-400 has the best surface hydrophilicity. The improvement of surface hydrophilicity can enable the electrolyte to effectively contact metal active sites on the catalyst surface. Thus, the adsorption of OH$^-$ and mass transfer efficiency of

reactants can be improved, which ultimately accelerates OER reaction kinetics and increases the electrocatalytic activity. Oxygen vacancies are defects formed by the removal of an oxygen atom from the lattice of a metal oxide. It is found that oxygen vacancies are more easily filled with OH$^-$ first on the surface of the oxygen vacancy-rich Co oxide, which facilitates the preoxidation of Co sites and the reconstruction/deprotonation of intermediaries (Co–OOH$^-$) during the OER process. Thus, oxygen vacancies can optimize the adsorption energy of the OH$^-$ intermediate on the catalyst surface, thus reducing the reaction energy barrier, promoting molecular activation, and finally enhancing the catalytic OER activity [23].

CONCLUSIONS

In this study, Co_3O_4 was synthesized by simple pyrolysis of $Co(OH)_2$ and calcined at 400°C. The obtained sample has more surface oxygen vacancies and the smallest overpotential (η = 321 mV) at j = 10 mA cm^{-2} in 1.0 mol L^{-1} KOH compared with the other Co_3O_4 samples. The dehydration process and formation of mesoporous structure result in the generation of maximum oxygen vacancies at 400°C. The enhanced catalytic OER activity of Co_3O_4-400 is due to the high oxygen vacancy content. Moreover, Co_3O_4-400 presents excellent performance in ORR and Zn-air batteries. This study introduces a facile and general pyrolysis strategy to obtain Co_3O_4 with optimized oxygen vacancy content from $Co(OH)_2$. Achieving maximum oxygen
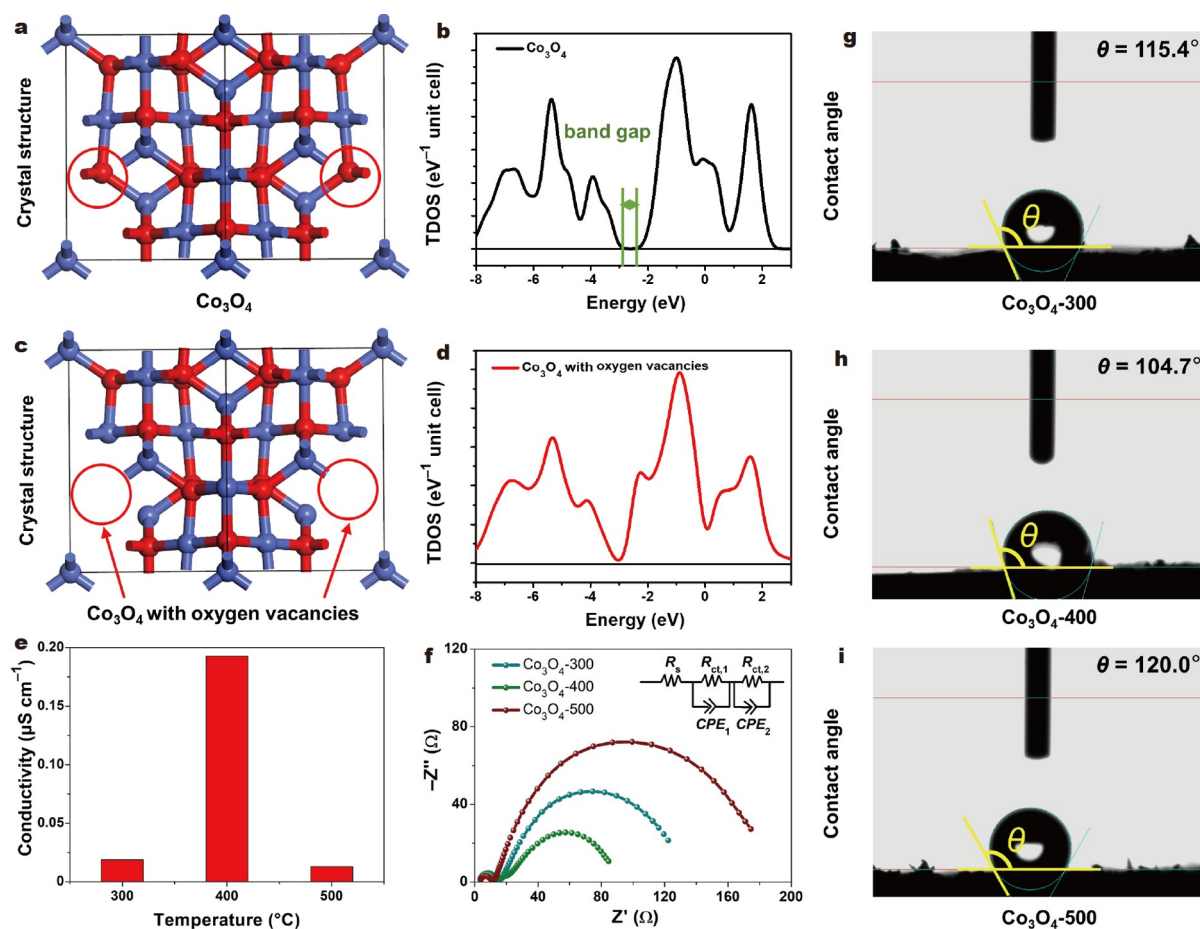
Figure 5 Crystal structures (a, c) and TDOS (b, d) of Co_3O_4 without and with oxygen vacancies. Electrical conductivity (e), EIS (f), and contact angles (g–i) of Co_3O_4-300, Co_3O_4-400, and Co_3O_4-500.

vacancy content in Co_3O_4 is of great importance and would be an important reference for designing and preparing other transition-metal oxides with rich oxygen vacancies from the corresponding metal hydroxides.

1 Mefford JT, Akbashev AR, Kang M, *et al.* Correlative *operando* microscopy of oxygen evolution electrocatalysts. Nature, 2021, 593: 67–73

2 Wu ZP, Lu XF, Zang SQ, *et al.* Non-noble-metal-based electrocatalysts toward the oxygen evolution reaction. Adv Funct Mater, 2020, 30: 1910274

3 Yang H, Han X, Douka AI, *et al.* Advanced oxygen electrocatalysis in energy conversion and storage. Adv Funct Mater, 2020, 31: 2007602

4 Wang HF, Tang C, Zhang Q. A review of precious-metal-free bifunctional oxygen electrocatalysts: Rational design and applications in Zn-air batteries. Adv Funct Mater, 2018, 28: 1803329

5 Liu P, Chen B, Liang C, *et al.* Tip-enhanced electric field: A new mechanism promoting mass transfer in oxygen evolution reactions. Adv Mater, 2021, 33: 2007377

6 Wang Y, Yang C, Huang Y, *et al.* Nickel induced electronic structural regulation of cobalt hydroxide for enhanced water oxidation. J Mater Chem A, 2020, 8: 6699–6708

7 Liang Z, Yang Z, Huang Z, *et al.* Novel insight into the epitaxial growth mechanism of six-fold symmetrical β-$Co(OH)_2$/$Co(OH)F$ hierarchical hexagrams and their water oxidation activity. Electrochim Acta, 2018, 271: 526–536

8 Wang Y, Zhu R, Wang Z, *et al.* Cu induced formation of dendritic CoFeCu ternary alloys on Ni foam for efficient oxygen evolution reaction. J Alloys Compd, 2021, 880: 160523

9 Wang Y, Han Y, Yan K, *et al.* Effects of Fe on electrocatalytic oxygen evolution reaction activity for CoFe layered double hydroxide nanosheets. J Alloys Compd, 2022, 903: 163994

10 Qi J, Lin YP, Chen D, *et al.* Autologous cobalt phosphates with modulated coordination sites for electrocatalytic water oxidation. Angew Chem Int Ed, 2020, 59: 8917–8921

11 Wang J, Cui W, Liu Q, *et al.* Recent progress in cobalt-based heterogeneous catalysts for electrochemical water splitting. Adv Mater, 2016, 28: 215–230

12 Liang Z, Yang C, Zhang W, *et al.* Anion engineering of hierarchical Co–A (A = O, Se, P) hexagrams for efficient electrocatalytic oxygen evolution reaction. Chin Chem Lett, 2021, 32: 3241–3244

13 Ge K, Sun S, Zhao Y, *et al.* Facile synthesis of two-dimensional iron/cobalt metal-organic framework for efficient oxygen evolution electrocatalysis. Angew Chem Int Ed, 2021, 60: 12097–12102

14 Li J, Liu Y, Chen H, *et al.* Design of a multilayered oxygen-evolution electrode with high catalytic activity and corrosion resistance for saline water splitting. Adv Funct Mater, 2021, 31: 2101820

15 Li X, Xiao L, Zhou L, *et al.* Adaptive bifunctional electrocatalyst of amorphous CoFe oxide@2D black phosphorus for overall water splitting. Angew Chem Int Ed, 2020, 59: 21106–21113

16 Kang W, Wei R, Yin H, *et al.* Unraveling sequential oxidation kinetics and determining roles of multi-cobalt active sites on Co_3O_4 catalyst for water oxidation. J Am Chem Soc, 2023, 145: 3470–3477

17 Wiegmann T, Pacheco I, Reikowski F, *et al. Operando* identification of the reversible skin layer on Co_3O_4 as a three-dimensional reaction zone for oxygen evolution. ACS Catal, 2022, 12: 3256–3268

18 Zeng H, Oubla M, Zhong X, *et al.* Rational defect and anion chemistries in Co_3O_4 for enhanced oxygen evolution reaction. Appl Catal B-Environ, 2021, 281: 119535

19 Xiao Z, Wang Y, Huang YC, *et al.* Filling the oxygen vacancies in Co_3O_4 with phosphorus: An ultra-efficient electrocatalyst for overall water splitting. Energy Environ Sci, 2017, 10: 2563–2569

20 Yan D, Li Y, Huo J, *et al.* Defect chemistry of nonprecious-metal electrocatalysts for oxygen reactions. Adv Mater, 2017, 29: 1606459

21 Xie C, Yan D, Li H, *et al.* Defect chemistry in heterogeneous catalysis: Recognition, understanding, and utilization. ACS Catal, 2020, 10:

22 Ji D, Fan L, Tao L, *et al.* The Kirkendall effect for engineering oxygen vacancy of hollow Co_3O_4 nanoparticles toward high-performance portable zinc-air batteries. Angew Chem Int Ed, 2019, 58: 13840–13844

23 Xiao Z, Huang YC, Dong CL, *et al. Operando* identification of the dynamic behavior of oxygen vacancy-rich Co_3O_4 for oxygen evolution reaction. J Am Chem Soc, 2020, 142: 12087–12095

24 Zhang R, Pan L, Guo B, *et al.* Tracking the role of defect types in Co_3O_4 structural evolution and active motifs during oxygen evolution reaction. J Am Chem Soc, 2023, 145: 2271–2281

25 Zhang N, Li X, Ye H, *et al.* Oxide defect engineering enables to couple solar energy into oxygen activation. J Am Chem Soc, 2016, 138: 8928–8935

26 Xu L, Jiang Q, Xiao Z, *et al.* Plasma-engraved Co_3O_4 nanosheets with oxygen vacancies and high surface area for the oxygen evolution reaction. Angew Chem Int Ed, 2016, 55: 5277–5281

27 Ma L, Chen S, Pei Z, *et al.* Flexible waterproof rechargeable hybrid zinc batteries initiated by multifunctional oxygen vacancies-rich cobalt oxide. ACS Nano, 2018, 12: 8597–8605

28 Li Z, Zhang Y, Feng Y, *et al.* Co_3O_4 nanoparticles with ultrasmall size and abundant oxygen vacancies for boosting oxygen involved reactions. Adv Funct Mater, 2019, 29: 1903444

29 Zhuang L, Ge L, Yang Y, *et al.* Ultrathin iron-cobalt oxide nanosheets with abundant oxygen vacancies for the oxygen evolution reaction. Adv Mater, 2017, 29: 1606793

30 Ling T, Yan DY, Jiao Y, *et al.* Engineering surface atomic structure of single-crystal cobalt(II) oxide nanorods for superior electrocatalysis. Nat Commun, 2016, 7: 12876

31 He D, Song X, Li W, *et al.* Active electron density modulation of Co_3O_4-based catalysts enhances their oxygen evolution performance. Angew Chem Int Ed, 2020, 59: 6929–6935

32 Ou G, Xu Y, Wen B, *et al.* Tuning defects in oxides at room temperature by lithium reduction. Nat Commun, 2018, 9: 1302

33 Wang Y, Yang C, Li Z, *et al.* The NH_x group induced formation of 3D α-$Co(OH)_2$ curly nanosheet aggregates as efficient oxygen evolution electrocatalysts. Small, 2020, 16: 2001973

34 Liang Z, Zhang C, Xu Y, *et al.* Dual tuning of ultrathin α-$Co(OH)_2$ nanosheets by solvent engineering and coordination competition for efficient oxygen evolution. ACS Sustain Chem Eng, 2018, 7: 3527–3535

35 Zhang R, Zhang YC, Pan L, *et al.* Engineering cobalt defects in cobalt oxide for highly efficient electrocatalytic oxygen evolution. ACS Catal, 2018, 8: 3803–3811

36 Gao R, Liu L, Hu Z, *et al.* The role of oxygen vacancies in improving the performance of CoO as a bifunctional cathode catalyst for rechargeable Li-O_2 batteries. J Mater Chem A, 2015, 3: 17598–17605

37 Liang Z, Huang Z, Yuan H, *et al.* Quasi-single-crystalline CoO hexagrams with abundant defects for highly efficient electrocatalytic water oxidation. Chem Sci, 2018, 9: 6961–6968

38 Wang ZL, Yin JS, Jiang YD. EELS analysis of cation valence states and oxygen vacancies in magnetic oxides. Micron, 2000, 31: 571–580

39 Li D, Wang H, Li K, *et al.* Emergent and robust ferromagnetic-insulating state in highly strained ferroelastic $LaCoO_3$ thin films. Nat Commun, 2023, 14: 3638

40 Xu W, Lyu F, Bai Y, *et al.* Porous cobalt oxide nanoplates enriched with oxygen vacancies for oxygen evolution reaction. Nano Energy, 2018, 43: 110–116

41 Bao J, Zhang X, Fan B, *et al.* Ultrathin spinel-structured nanosheets rich in oxygen deficiencies for enhanced electrocatalytic water oxidation. Angew Chem Int Ed, 2015, 54: 7399–7404

42 Huang Y, Li M, Pan F, *et al.* Plasma-induced Mo-doped Co_3O_4 with enriched oxygen vacancies for electrocatalytic oxygen evolution in water splitting. Carbon Energy, 2023, 5: e279

43 Li M, Wang X, Liu K, *et al.* Reinforcing Co–O covalency *via* Ce(4f)–O(2p)–Co(3d) gradient orbital coupling for high-efficiency oxygen evolution. Adv Mater, 2023, 35: 2302462

44 Wang Y, Suo W, Huang Y, *et al.* Defect structure regulation and mass transfer improvement of cobalt-based oxides for enhanced oxygen evolution reaction. J Alloys Compd, 2022, 928: 167210

45 Yu F, Liu Z, Li Y, *et al.* Effect of oxygen vacancy defect regeneration on

photocatalytic properties of ZnO nanorods. Appl Phys A, 2020, 126: 931

46 Liang Z, Kong N, Yang C, et al. Highly curved nanostructure-coated Co, N-doped carbon materials for oxygen electrocatalysis. Angew Chem Int Ed, 2021, 60: 12759–12764

47 Yeo BS, Bell AT. Enhanced activity of gold-supported cobalt oxide for the electrochemical evolution of oxygen. J Am Chem Soc, 2011, 133: 5587–5593

48 Wan S, Qi J, Zhang W, et al. Hierarchical Co(OH)F superstructure built by low-dimensional substructures for electrocatalytic water oxidation. Adv Mater, 2017, 29: 1700286

49 Bajdich M, García-Mota M, Vojvodic A, et al. Theoretical investigation of the activity of cobalt oxides for the electrochemical oxidation of water. J Am Chem Soc, 2013, 135: 13521–13530

50 Costentin C, Porter TR, Savéant JM. Conduction and reactivity in heterogeneous-molecular catalysis: New insights in water oxidation catalysis by phosphate cobalt oxide films. J Am Chem Soc, 2016, 138: 5615–5622

51 Liang Z, Guo H, Zhou G, et al. Metal-organic-framework-supported molecular electrocatalysis for the oxygen reduction reaction. Angew Chem Int Ed, 2021, 60: 8472–8476

52 Li X, Wei J, Li Q, et al. Nitrogen-doped cobalt oxide nanostructures derived from cobalt-alanine complexes for high-performance oxygen evolution reactions. Adv Funct Mater, 2018, 28: 1800886

Author contributions Wang Y conceived the idea and wrote the original manuscript. Han Y performed the experiments. Suo W analyzed the data. Zhang J revised the manuscript with support from Lai X, Li Z and Liang Z. Cao G contributed to the supervision and project administration. All authors contributed to the general discussion.

Conflict of interest The authors declare that they have no conflict of interest.

Supplementary information Supporting data are available in the online version of the paper.

Yuan Wang joined the School of Advanced Materials and Nanotechnology, Xidian University in 2016. Now, she is an associate professor of Huashan Scholar Elite at Xidian University. Her research is focused on the development of high-efficiency electrodes for energy and electronic information fields and electronic functional materials & devices.

Zhimin Li received his PhD degree in materials science from the Northwestern Polytechnical University in 2008. He worked at the National Institute for Materials Science (NIMS) in Japan from July 2010 to July 2011 as a post-doctoral research fellow. He is now a professor at the School of Advanced Materials and Nanotechnology, Xidian University. His current research interest is dielectric materials, and energy materials and devices.

Zuozhong Liang is currently an associate research fellow at the School of Chemistry and Chemical Engineering, Shaanxi Normal University. He received his BS degree (2011) from Qufu Normal University and PhD degree (2016) from Beijing University of Chemical Technology under the supervision of Professor Jian-Feng Chen. In July 2016, he joined Professor Rui Cao's research group. His research interests are the design and development of novel functional nanomaterials for the applications in renewable-energy-related fields.

Guozhong Cao is a Boeing-Steiner Professor of materials science and engineering, professor of chemical engineering, and adjunct professor of mechanical engineering at the University of Washington, and also a professor at Beijing Institute of Nanoenergy and Nanosystems, Chinese Academy of Sciences and Dalian University of Technology. His current research is focused on chemical processing of nanomaterials for energy-related applications including solar cells, rechargeable batteries, supercapacitors, and hydrogen storage.

具有峰值氧空位含量的过渡金属氧化物用于氧电催化

王媛[1], 韩玉[1], 索伟然[1], 张洁灵[2], 赖小勇[3], 李智敏[1*], 梁作中[2*], 曹国忠[4*]

摘要 在过渡金属氧化物中引入氧空位是提高电催化性能的有效途径. 然而, 控制金属氧化物的缺陷工程仍然面临挑战. 在此, 我们报道了一种通过调节热解温度制备相应的金属氧化物来反映氧空位含量峰值的方法. 具体来说, $Co(OH)_2$在空气中400°C热解生成的Co_3O_4纳米花具有最多的氧空位. 大量氧空位含量的产生可能是由于丰富的多孔结构和Co和O原子的重排过程导致的. 电化学结果表明, 在$1.0\ mol\ L^{-1}$ KOH条件下, 当电流密度j = 10 mA cm^{-2}时, 在400°C条件下制备的富氧空位缺陷的Co_3O_4 (Co_3O_4-400)与Co_3O_4-300 (348 mV)和Co_3O_4-500 (366 mV)相比, 析氧反应的过电位η最低, 为321 mV. 理论计算和实验证实了Co_3O_4中氧空位的有利作用. 本研究为开发具有优化氧空位的高活性过渡金属氧化物提供了新的见解.